

# ShortcutBreaker: Low-Rank Noisy Bottleneck and Frequency Filtering Block for Multi-Class Unsupervised Anomaly Detection

Peng Tang<sup>1</sup> Xiaobin Hu<sup>2</sup> Yang Nan<sup>3</sup> Tingcheng Li<sup>4</sup> Tobias Lasser<sup>1</sup> Hongwei Bran Li<sup>2</sup>

## Abstract

Multi-class Unsupervised Anomaly Detection (MUAD) has attracted increasing research interest for its ability to develop a unified model across multiple classes, significantly reducing the computational cost of training separate models for distinct objects. However, despite the performance gains offered by advanced Transformer-based architectures, the identity shortcut issue persists. These models tend to directly copy inputs to outputs, narrowing the reconstruction error gap between normal and abnormal cases and hindering distinguishability. To address this, we propose ShortcutBreaker, a framework designed to disrupt such shortcuts through two core innovations. First, we introduce a Low-Rank Noisy Bottleneck (LRNB) derived from matrix rank inequality, which theoretically prevents trivial identity mapping by perturbing features across two distinct reconstruction groups. Second, we design a Frequency-Filter Unit (FFU) that integrates frequency spectral filtering and global-local masking. This mechanism further enlarges the anomaly score gap, with less computational cost than standard self-attention. Extensive evaluations on four benchmarks (MVTec-AD, ViSA, Real-IAD, and Universal Medical) demonstrate the superiority of ShortcutBreaker. Our code will be released.

## 1. introduction

Anomaly detection in industrial and medical imaging aims to identify abnormal patterns among normal cases, saving labor and time in collecting and labeling anomalies. Given the abundance of normal cases and the scarcity of anomalies, this task is typically tackled via an unsupervised paradigm using only normal training samples.

<sup>1</sup>TUM <sup>2</sup>NUS <sup>3</sup>imperial college London <sup>4</sup>Suzhou University of Science and Technology. Correspondence to: Xiaobin Hu < >.

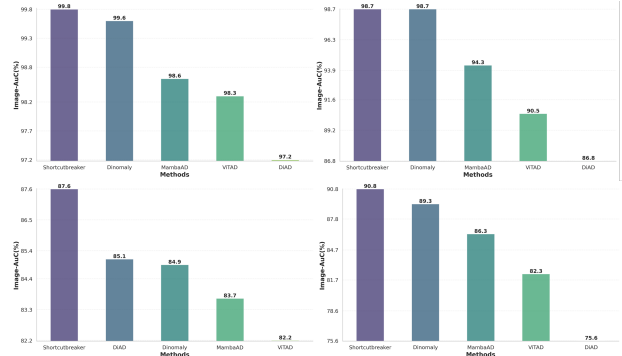


Figure 1. Performance comparison in terms of image-level AUC on MVTEC, ViSA, Universal Medical and Real-IAD.

Before deep learning, anomaly detection relied on traditional techniques: density-based methods (Breunig et al., 2000; Guan et al., 2015), distance-based methods (Knorr et al., 2000; Angiulli et al., 2005), and statistics-based methods (Hido et al., 2011; Rousseeuw & Hubert, 2011). Current state-of-the-art methods employ deep learning networks pre-trained on ImageNet (Deng et al., 2009) to capture discriminative features. Feature reconstruction methods (Guo et al., 2023; 2024; Deng & Li, 2022) reconstruct encoder-extracted features, assuming accurate reconstruction of normal regions but failure on unseen anomalies. Memory matching methods (Yi & Yoon, 2020; Defard et al., 2021; Roth et al., 2022) memorize training-set normal features for inference matching, with those in (Defard et al., 2021; Roth et al., 2022) using pre-trained encoders for discriminative features. Pseudo-anomaly methods (Liu et al., 2023; Li et al., 2021; Zavrtnik et al., 2021) convert UAD to a supervised task by generating pseudo anomalies via noise addition to normal images/features. Hybrid methods (Tien et al., 2023; Zhao et al., 2023) integrate normalizing flows (Zhao et al., 2023) or pseudo noise (Tien et al., 2023) into feature reconstruction for UAD.

Despite their success, these methods are limited to a one-model-one-class setup, requiring substantial storage for per-class models—especially with many disease types (You et al., 2022). To address this, UniAD and follow-ups propose unified models for multi-class unsupervised anomaly detection (MUAD). However, identity mapping often emerges here, where the model returns input copies re-

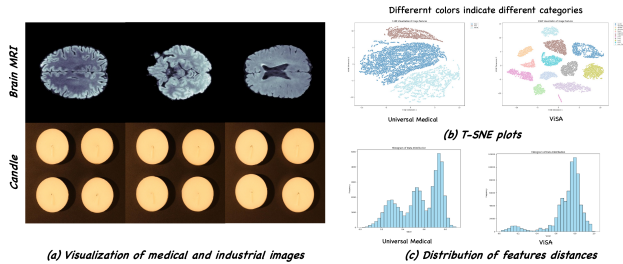


Figure 2. The visual patterns in the medical field are richer than those in the industrial field. (a) Visualization results (b) T-SNE plots (Van der Maaten & Hinton, 2008), and (c) distributions of feature distances for the Universal Medical and ViSA datasets (Zou et al., 2022) are presented. These experimental results help observe the diversity of each dataset. For T-SNE plots, we extract the final features from the pre-trained ResNet-50 (He et al., 2016). Moreover, we use LPIPs (Zhang et al., 2018) to compare feature distances between individual image pairs.

ardless of normality, enabling effective reconstruction of even anomalous samples and hindering detection (You et al., 2022).

Over the past three years, substantial progress has been made in multi-class unsupervised anomaly detection (MUAD), with explorations into pretrained vision transformers (ViTs) (Zhang et al., 2023; Guo et al., 2025), state space models (Mambas) (He et al., 2024a), diffusion models (Yin et al., 2023; He et al., 2024b), and other approaches (Guo et al., 2024; Zhao, 2023; He et al., 2024c). Nevertheless, the multi-class setting inevitably induces identity mapping in most methods, resulting in performance degradation. While previous studies (You et al., 2022; Guo et al., 2025) have endeavored to mitigate shortcut learning, the efficacy of their proposed techniques in complex and highly diverse scenarios remains limited (see Fig. 1 (c)-(d)). This is particularly evident in datasets such as Real-IAD and Universal Medical, where the abundance of normal patterns exacerbates the aforementioned issue (You et al., 2022). The effectiveness of simple noise operations (You et al., 2022; Guo et al., 2025) is diminished due to the enhanced noise robustness acquired through exposure to diverse visual patterns. Consequently, to enhance performance, our work aims to efficiently address the problem of identity shortcuts. Furthermore, why are the Real-IAD and Universal Medical datasets more complex? We elaborate on this as follows: It is apparent that in comparison to widely adopted industrial datasets—MVTec-AD (encompassing 15 classes) (Bergmann et al., 2019) and ViSA (comprising 12 classes) (Zou et al., 2022)—Real-IAD (Wang et al., 2024) exhibits more diverse normal patterns, featuring 30 object categories and 5 camera views. In contrast to standardized industrial images, although the Universal Medical dataset (He et al., 2024b) consists of only 3 categories, the inherent heterogeneity within medical normal samples enriches the visual features (e.g., variations in organ size and shape across different demographics, as illustrated in Fig. 2(a)). Moreover,

the Universal Medical dataset displays a sparser t-SNE plot and a wider dispersion of feature distances compared to ViSA (see Fig. 2 (b) and (c)), indicating a higher degree of intrinsic diversity within medical data.

In this paper, we propose a simple yet effective framework for the MUAD task, named ShortcutBreaker, built on the advanced DINO-pretrained vision transformer with two key innovations. First, drawing on two observed properties of low-rank matrix decomposition, we design a low-rank noisy bottleneck (LRNB) to effectively mitigate the identity mapping issue. Within LRNB, the low-rank property theoretically circumvents shortcut learning of unseen patterns, while learnable matrix parameters are optimized to reconstruct normal patterns. Second, we introduce a Frequency-Filter Unit (FFU) to replace self-attention, which efficiently curbs information leakage from input to output in the frequency domain. In FFU, a frequency spectral filtering and a local masking mechanism are integrated, forcing the decoder to learn reconstruction based on longer-range and impaired features.

To validate the effectiveness of the proposed method, we conduct extensive experiments on four publicly available datasets: MVTec-AD (Bergmann et al., 2019), ViSA (Zou et al., 2022), Universal Medical (He et al., 2024b), and Real-IAD (Wang et al., 2024). As presented in Fig. 1, our ShortcutBreaker achieves the highest image-level AUC: 99.8%, 98.9%, 88.2%, and 90.6% on these four datasets, respectively. Notably, on the complex Universal Medical and Real-IAD datasets, it outperforms previous methods by a significant margin. In summary, our contributions are:

- We observe and simulate the properties of matrix decomposition to design a low-rank noisy bottleneck, efficiently suppressing identity mapping.
- We propose a frequency-filtering unit that integrates frequency spectral filtering and global-local masking operations, detecting anomalies more efficiently than standard self-attention.
- Our ShortcutBreaker consistently outperforms previous methods across all four datasets, demonstrating enhanced robustness in diverse scenarios.

### 1.1. Multi Class UAD

UniAD (You et al., 2022) pioneers the field of multi-class unsupervised anomaly detection (MUAD), presenting a unified model capable of detecting anomalies across various classes. Most subsequent works have explored advanced modules to build better reconstruction models for MUAD. For example, LafitE (Yin et al., 2023) and DiAD (He et al., 2024b) further advance the MUAD task by leveraging the generative power of diffusion models to better capture anomalies

across multiple classes. ViTAD (Zhang et al., 2023) and MambaAD (He et al., 2024a) develop feature reconstruction-based MUAD methods using recently advanced modules: Vision Transformer (Zhang et al., 2023) and State Space Model (He et al., 2024a), respectively. Few methods explicitly aim to address the identity mapping issue. UniAD (You et al., 2022) counteracts this through techniques like feature jittering and neighbor-masked attention. Dinomaly (Guo et al., 2025) employs components such as noisy bottleneck dropout to disrupt input feature replication. However, these noise operations have limited effectiveness in preventing shortcut learning when training on complex medical/industrial datasets (Universal Medical and Real-IAD).

## 2. Method

### 2.1. Overview

Following ViTAD and Dinomaly (Zhang et al., 2023; Guo et al., 2025), our ShortcutBreaker is a feature-reconstruction framework and is constructed based on the vision transformer (ViT) structure. As depicted in Fig. 3(a), ShortcutBreaker consists of a pre-trained encoder, a bottleneck, and a decoder. The DINO-pretrained ViT model (Darcet et al., 2023) is utilized as the encoder, capturing informative feature tokens to facilitate subsequent reconstruction. The bottleneck is built upon a multi-layer perceptron (MLP), integrating multi-scale feature representations from intermediate encoder layers. The decoder based on frequency-filtering blocks maintains structural similarity with the encoder, employing transformer layers to reconstruct feature maps. As illustrated in Fig. 3(d), the encoder remains frozen during training, while the remaining components of ShortcutBreaker are optimized to reconstruct the encoder’s feature tokens by minimizing inter-token representation discrepancies. During inference, this configuration enables accurate reconstruction of normal patterns but exhibits reconstruction failures in anomalous regions. The anomaly localization map is generated by computing 1-CS (where CS denotes cosine similarity) between the original and reconstructed feature tokens and then reshaping the result. The anomaly detection score is subsequently determined by the maximum value within this anomaly map.

### 2.2. Low-Rank Noisy Bottleneck (LRNB)

As discussed in the introduction, under the MUAD setting, identity shortcuts readily occur, narrowing the gap in anomaly scores between normal and abnormal cases. Previous methods (Guo et al., 2025; You et al., 2022) propose perturbing extracted feature tokens to compel the network to reconstruct from information-impaired normal features, rather than directly copying them. However, these noisy operations are often limited in effectively preventing shortcut learning in complex scenarios. We hypothesize that richer vi-

sual patterns inherent in the data enhance the reconstruction model’s robustness to stochastic noise. Consequently, we aim to design a novel paradigm for avoiding shortcuts that goes beyond solely relying on noisy operations. Through empirical observation of low-rank matrix decomposition in LoRA (Hu et al., 2022) (or the encoder-decoder structure in Auto-Encoder (He et al., 2022)), we identified two inherent properties particularly suitable for addressing the identity mapping issue.

**Property 1** This property stems from the constrained low-rank latent space, which effectively circumvents identity shortcuts. In deep learning, nonlinear activations are generally used to improve performance, so we introduce the tool of the Jacobian matrix (Goodfellow et al., 2016) to conduct a linear approximation for the proof of this property. Given that the feature tokens extracted from DINO-v2 are highly informative, we assume them to be full-rank.

To achieve identity mapping of  $x \in \mathbb{R}^d$ , we require that  $g \circ f(x) = x$  holds for all  $x \in \mathbb{R}^n$ . Differentiating both sides with respect to  $x$  yields the Jacobian equation:

$$J_g(f(x)) \cdot J_f(x) = I_{d \times d} \tag{1}$$

where  $J_f(x) \in \mathbb{R}^{d \times k}$  and  $J_g(f(x)) \in \mathbb{R}^{k \times d}$ . Taking the determinant of both sides:

$$r((J_g(f(x)) \cdot J_f(x))) = r(I_{d \times d}) = d. \tag{2}$$

Since the product  $J_g(f(x)) \cdot J_f(x)$  is an  $d \times d$  matrix, applying the rank inequality yields:

$$r(J_g(f(x)) \cdot J_f(x)) \leq \min(r(J_g(f(x))), r(J_f(x))) \leq k \tag{3}$$

Here,  $r(\cdot)$  indicate the rank of the input. Under the low-rank adaptation module, we have  $k < d$ . Substituting into Eq. (3) implies:

$$r(J_g(f(x)) \cdot J_f(x)) \leq k < d \tag{4}$$

This contradicts Eqs. (2) that  $\det(I_{d \times d})$  requires rank= $d$ . Consequently, no such functions  $f$  and  $g$  exist.

**Property 2** Property 1 prevents the identity mapping of all the inputs; however, our final goal is a favorable score trade-off between normal and abnormal samples. The property 2 emerges from training exclusively on normal samples, during which the learnable  $g$  and  $f$  layers are optimized to specifically enhance the reconstruction of normal patterns. This optimization process minimizes adverse effects on the reconstruction fidelity of normal cases, thereby enlarging the gap of reconstruction errors between the two types of samples.

Specifically, functions  $g$  and  $f$  are parameterized by Multi-Layer Perceptrons (MLPs) with GeLU activations. As illustrated in Fig. 3,  $g$  and  $f$  feature symmetric architectures consisting of  $L$  downsampling (DB) and upsampling blocks

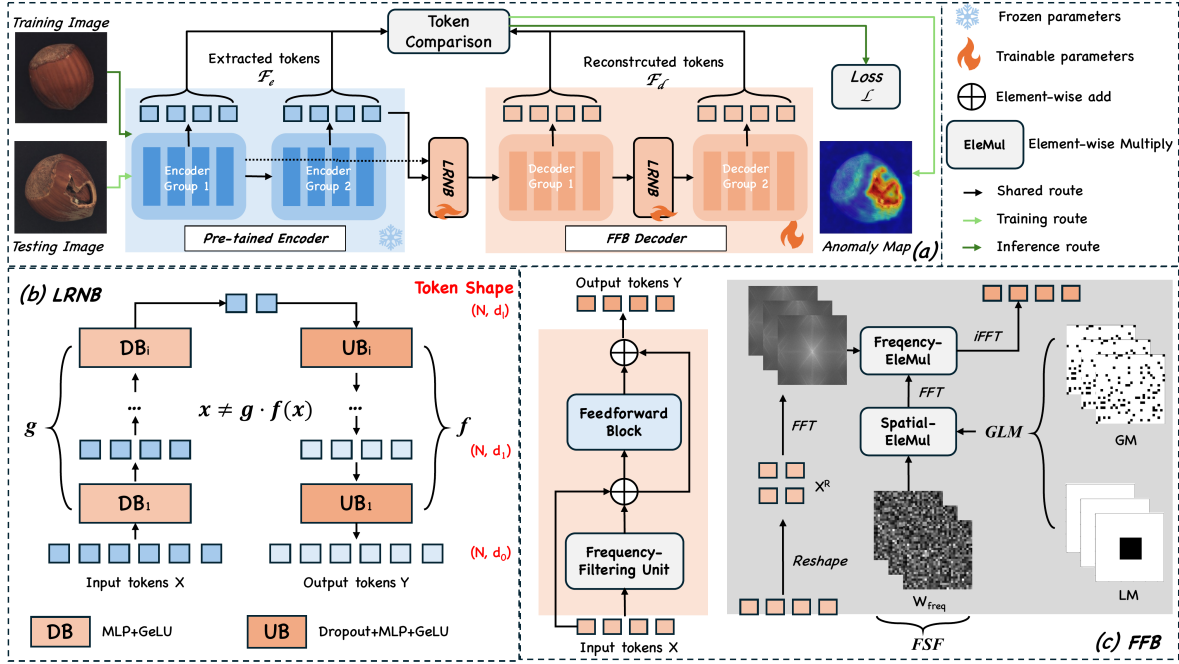


Figure 3. Flowchart of our ShortcutBreaker: (a) the overall structure of our proposed method; (b) the structure of the Low-Rank Noisy Bottleneck (LRNB); (c) the structure of the Frequency-Filtering Block (FFB), which consists of a Frequency-Filtering Unit and a Feedforward block. FFT: Fast Fourier Transform, iFFT: Inverse Fast Fourier Transform, FSF: frequency spectral filtering, LM: local masking  $M_l$ , and GM: global masking  $M_g$ .

(UB), respectively. Within these modules, each DB reduces the token dims by low-rank ratio  $r$ , (i.e.,  $d_i = d_{i-1}/r$ , sequence length  $n$  remains unchanged), while UBs correspondingly scale it back. To reinforce feature-level perturbation, Dropout (Guo et al., 2025) is integrated into the UBs. Furthermore, departing from existing methods that employ a single noise bottleneck, we deploy dual LRNBs—injecting one before each of the two decoder groups—to perturb reconstruction.

### 2.3. Frequency-Filtering Block

The self-attention mechanism is the core component of Transformer, as shown in Eq. 5, enabling the model to focus on different parts of the input tokens.

$$\text{Attention}(Q, K, V) = \text{Softmax}\left(\frac{QK^T}{\sqrt{d}}\right)V = A(X)V \tag{5}$$

where  $Q \in \mathbb{R}^{N \times d}$ ,  $K \in \mathbb{R}^{N \times d}$  and  $V \in \mathbb{R}^{N \times d}$  are projected from input tokens  $X \in \mathbb{R}^{N \times d}$ , indicating the query, key and value vectors respectively.  $K^T \in \mathbb{R}^{d \times N}$  is the transpose matrix of  $K$  and  $d_k$  is the scaling factor.

In anomaly detection, Transformer blocks have recently been adopted to replace conventional convolution blocks due to their global modeling capability (You et al., 2022; Zhang et al., 2023; Guo et al., 2025). However, the self-attention mechanism often learns a “spiky” weight distribution, primarily focusing on the query’s own location, which

facilitates an identity shortcut (You et al., 2022; Guo et al., 2025).

Motivated by three intuitive benefits, we construct a Frequency-Filtering Block (FFB) by replacing the self-attention mechanism by a Frequency-Filtering Unit, as shown in Fig. 3(c). **First**, the FFU processes token sequences in the frequency domain using the 2D DFT. According to the properties of the DFT, every spectral coefficient encapsulates information from all spatial locations. By performing mixing in this spectral space, the FFU inherently maintains a holistic global modeling capability, forcing the model to reconcile inputs with a global distribution. This effectively prevents the network from relying on isolated localized shortcuts for reconstruction. **Second**, unlike standard self-attention  $A(X) = \text{Softmax}(QK^T/\sqrt{d})$ , where input-dependent  $Q$  and  $K$  matrices are prone to optimizing for increased spectral norms—causing  $A(X)$  to collapse into an identity matrix ( $A(X) \approx I$ ) and creating an identity shortcut for anomalies—the FFU mitigates this issue through its input-independent architecture. The spectral filter (see  $W_{freq}$  in Fig. 3) consists of learnable parameters that remain fixed during inference. During training, it learns a static spectral template representing the global energy distribution of normal patterns and cannot dynamically “re-focus” its weights on unseen anomalous signals. **Third**, while self-attention incurs a quadratic computational cost of  $O(N^2 \cdot d)$  that bottlenecks memory and throughput, the FFU leverages the Fast Fourier Transform (FFT) to achieve

$O(N \log N \cdot d)$  complexity.

Eq. 6 defines the core FFU operation. The input sequence  $\mathbf{X} \in \mathbb{R}^{N \times d}$  is reshaped into a 2D representation  $\mathbf{X}^R \in \mathbb{R}^{H \times W \times d}$ , projected into the frequency domain via a 2D Discrete Fourier Transform (DFT),  $\mathcal{F}$ , and modulated through element-wise multiplication with a learnable, input-independent spectral filter  $\mathbf{W}_{freq}$ . The modulated features are then restored to the spatial domain using an Inverse DFT ( $\mathcal{F}^{-1}$ ). Furthermore, we introduce a Global and Local Masking (GLM) mechanism on  $\mathbf{W}_{freq}$  to suppress shortcut learning. local-masking (LM) mechanism prevents tokens from attending to their own positions. Considering the global modeling strength of FFU and ViT, all tokens in the same sequence may share similar information, we propose to mask tokens globally and randomly. Specifically, by the convolution theorem, frequency-domain multiplication corresponds to spatial circular convolution:

$$\mathbf{Y} = \text{FFU}(\mathbf{X}) = \mathcal{F}^{-1}(\mathcal{F}(\mathbf{X}^R) \odot \mathbf{W}_{freq}) = \mathbf{X}^R \otimes k \quad (6)$$

where  $k = \mathcal{F}^{-1}(\mathbf{W}_{freq})$  represents the spatial kernel,  $\odot$  denotes the element-wise multiplication,  $\otimes$  indicates the convolution operation. As shown in Fig. 3(c), we set the origin of  $k$  to zero (Local Masking) to prevent self-reproduction and apply Dropout on  $k$  (Global Masking) to impair the copy from other tokens. The constrained spectral filter  $\mathbf{W}_{freq}^M$  is then derived as:

$$\mathbf{W}_{freq}^M = \mathcal{F}(k \odot M_{local} \odot M_{global}) \quad (7)$$

The final formulated FFU is expressed as:

$$\text{FFU}(\mathbf{X}) = \mathcal{F}^{-1}(\mathcal{F}(\mathbf{X}^R) \odot \mathbf{W}_{freq}^M) \quad (8)$$

### 3. Experiments

#### 3.1. Experimental Setting

**Datasets** We evaluated our method on four well-established datasets, including three for industrial scenarios: **MVTec-AD** (Bergmann et al., 2019), **ViSA** (Zou et al., 2022), **Real-IAD** (Wang et al., 2024), and one for medical scenario: **Universal Medical** (He et al., 2024b;a; Zhang et al., 2023; 2024). **MVTec-AD** comprises 15 object categories, with 3,629 normal images in the training set and 498 normal images alongside 1,982 anomalous samples in the test set. **ViSA** contains 12 categories, providing 8,659 normal training images and a test set with 962 normal images and 1,200 anomalous cases. **Real-IAD**, the largest industrial benchmark, includes 30 diverse objects, utilizing 36,645 normal images for training and 63,256 normal images combined with 51,329 anomalous instances for testing. **Universal Medical** consists of 13,339 normal cases for training, with a test set containing 2,514 normal cases and 4,499 abnormal cases. This dataset spans three medical imaging modalities:

Brain MRI, Liver CT, and Retinal CT scans. All datasets include both image-level and pixel-level labels. **Metrics** For evaluation metrics, we followed protocols from (Zhang et al., 2023; He et al., 2024a; Guo et al., 2025), adopting four metrics: Area Under the Receiver Operating Curve (AUC), F1-max score, average precision (AP) for both image-level detection and pixel-level localization tasks, and Area Under the Per-Region-Overlap (AUPRO) to further evaluate the localization task. **Implementation details** In our experiments, the encoder is initialized with DINO pre-trained weights (Darcet et al., 2023) and kept frozen during training. Images are resized to 448×448 and then center-cropped to 392×392. We use a stable variant of the AdamW optimizer (Wortsman et al., 2023) incorporating the AMSGrad algorithm (Reddi et al., 2019), with a batch size of 32. Training iterations are set to 20,000 for all four datasets. The learning rate is initialized to 2e-3 and gradually reduced to 2e-4 via a Cosine Annealing schedule with a warm-start scheme (Loshchilov & Hutter, 2016). The model is optimized using the global hard-mining loss (Guo et al., 2025). In LRNB, we set the noise rate to 0.4 and the  $r$  to 4. Similar to Dinomaly, set the number of LRNB layers to 1 for MVTEC-AD and ViSA datasets, and 2 for more complex Universal Medical and Real-IAD datasets.

#### 3.2. Evaluations

**Comparison with SOTA MUAD methods** We evaluate our method against seven state-of-the-art (SOTA) MUAD methods—UniAD (You et al., 2022), DiAD (He et al., 2024b), ViTAD (Zhang et al., 2023), Recontrast (Guo et al., 2024), and Dinomaly (Guo et al., 2025)—across four benchmark datasets: MVTEC-AD (Bergmann et al., 2019), ViSA (Zou et al., 2022), Universal Medical (He et al., 2024b), and Real-IAD (Wang et al., 2024). Performance is quantified using both image-level metrics (I-AUC, I-AP, I-F1) and pixel-level metrics (P-AUC, P-AP, P-F1, P-AUPRO), where higher values indicate better detection capability. Experimental results are presented in Table 1, where our method outperforms comparative methods across all datasets in most metrics (The qualitative results obtained by our method can be seen in Fig. 4). On the widely adopted MVTEC-AD, our method achieves SOTA overall performance, with the highest image-level metrics of **99.8/99.9/99.4**, and pixel-level metrics of **98.5/71.5/70.5/95.6**. On ViSA, our method consistently achieves the superior overall performance, i.e., image-level metrics of **98.7/98.9/95.9** and pixel-level metrics of **99.0/53.9/55.0/94.5**. These results demonstrate that image-level performance on these two datasets is nearly 100%, making performance improvements subtle. On Universal Medical, our method attains the highest image-level metrics of **87.6/87.0/82.5**, surpassing prior SOTAs by a large margin of 2.7/2.9/1.5, and achieves best or second-best pixel-level metrics of **97.1/56.0/55.6/87.3**. On Real-

**ShortcutBreaker: Low-Rank Noisy Bottleneck and Frequency Filtering Block for Multi-Class Unsupervised Anomaly Detection**

Table 1. Comparison between our method and currently state-of-the-art methods on four datasets, MVTec-AD (Bergmann et al., 2019), ViSA (Zou et al., 2022), Universal Medical (He et al., 2024b) and Real-IAD (Wang et al., 2024). Bold values indicate the best, and underlined values indicates the second best. (%)

Method	MVTec-AD							ViSA						
	Image-Level			Pixel-Level				Image-Level			Pixel-Level			
	AUC	AP	F1	AUC	AP	F1	AUPRO	AUC	AP	F1	AUC	AP	F1	AUPRO
UniAD	96.5	98.8	96.2	96.8	43.4	49.5	90.7	88.8	90.8	85.8	98.3	33.7	39.0	85.5
Reconstrast	98.3	99.4	97.6	97.1	60.2	61.5	93.2	95.5	96.4	92.0	98.5	47.9	50.6	91.9
ViTAD	98.3	99.4	97.3	97.7	55.3	58.7	91.4	90.5	91.7	86.3	98.2	36.6	41.1	85.1
DiAD	97.2	99.0	96.5	96.8	52.6	55.5	90.7	86.8	88.3	85.1	96.0	26.1	33.0	75.2
MambaAD	98.6	99.6	97.8	97.7	56.3	59.2	93.1	94.3	94.5	89.4	98.5	39.4	44.0	91.0
Dinomaly	<u>99.6</u>	<u>99.8</u>	<u>99.0</u>	<u>98.4</u>	<u>69.3</u>	<u>69.2</u>	<u>94.8</u>	<b>98.7</b>	<b>98.9</b>	<b>96.2</b>	<u>98.7</u>	<u>53.2</u>	<b>55.7</b>	<b>94.5</b>
<b>Ours</b>	<b>99.8</b>	<b>99.9</b>	<b>99.4</b>	<b>98.5</b>	<b>71.5</b>	<b>70.5</b>	<b>95.6</b>	<b>98.7</b>	<b>98.9</b>	<u>95.9</u>	<b>99.0</b>	<b>53.9</b>	<u>55.0</u>	<b>94.5</b>

Method	Universal Medical							Real-IAD						
	Image-Level			Pixel-Level				Image-Level			Pixel-Level			
	AUC	AP	F1	AUC	AP	F1	AUPRO	AUC	AP	F1	AUC	AP	F1	AUPRO
UniAD	78.5	75.2	76.6	96.4	37.6	40.2	85.0	83.0	80.9	74.3	97.3	21.1	29.2	86.7
Reconstrast	80.1	79.7	80.9	96.3	42.3	43.8	85.2	86.4	84.2	77.4	97.8	31.6	38.2	91.8
ViTAD	82.2	81.0	80.1	<b>97.1</b>	49.9	49.6	86.1	82.3	79.4	73.4	96.9	26.7	34.9	84.9
DiAD	<u>85.1</u>	<u>84.5</u>	81.2	95.9	38.0	35.6	85.4	75.6	66.4	69.9	88.0	2.9	7.1	58.1
MambaAD	83.7	80.1	<u>82.0</u>	<u>96.9</u>	45.4	47.3	<b>87.5</b>	86.3	84.6	77.0	98.5	33.0	38.7	90.5
Dinomaly	84.9	84.1	81.0	96.8	<u>51.7</u>	<u>52.1</u>	85.5	<u>89.3</u>	<u>86.8</u>	<u>80.2</u>	<u>98.8</u>	<u>42.8</u>	<u>47.1</u>	<u>93.9</u>
<b>Ours</b>	<b>87.6</b>	<b>87.0</b>	<b>82.5</b>	<b>97.1</b>	<b>56.0</b>	<b>55.6</b>	<u>87.3</u>	<b>90.8</b>	<b>88.2</b>	<b>81.5</b>	<b>98.9</b>	<b>46.6</b>	<b>49.7</b>	<b>95.0</b>

IAD, our method produces a new SOTA result, with image-level and pixel-level performance of **90.8/88.2/81.5** and **98.9/46.6/49.7/95.0**, outperforming previous SOTAs by 1.5/1.4/1.3 and 0.1/3.4/2.6/1.1. These results demonstrate strong generalization to complex medical and diverse real-world industrial scenarios.

**3.3. Ablation Studies**

**Overall Ablation** To explore the contributions of each component in our method, including the low-rank noisy bottleneck (LRNB), global filtering (GF), and global-local masking (GLM) operations, we conduct ablation experiments as shown in Table 2. The baseline is constructed following Dinomaly (Guo et al., 2025) and ViTAD (Zhang et al., 2023), which construct a baseline model with a DINO-pretrained ViT encoder and a learnable softmax attention-based ViT decoder. The effectiveness of the baseline has been proven in industrial scenarios. The results of the ablation experiments demonstrate that the proposed LRNB, GF and GLM modules all contribute to performance improvement, with their combinations further enhancing performance. Compared to the baseline model, using any single module alone achieves better performance in terms of the key indicators I-AUC and

P-AUC. Among them, FFB (GF with GLM) brings moderate improvements, while LRNB shows the most significant enhancement—it notably boosts image-level and pixel-level performances with respective large margins of 5.1/6.9/5.7 and 2.3/13.9/9.9/3.6 on Real-IAD dataset and 1.1/0.7/1.6, and 1.1/8.4/6.9/1.9 on MvTec-AD dataset. These results demonstrate that the LRNB module serves as a core foundation in our method. When replacing self-attention with sole GF, the overall improvements on two datasets are subtle, however the computational complexity is reduced from  $O(N^2 \cdot d)$  to  $O(N \log N \cdot d)$ . Further combination with GLM yields even better results. The final integration of all three modules (LRNB + GF + GLM) delivers the best overall performance, achieving the highest image-level and pixel-level metrics on both datasets—confirming that their collaborative effect effectively enhances the model’s overall performance.

Table 3 illustrates the impact of dual injection within the LRNB framework. The results demonstrate that injecting LRNB before either the Group 1 (G1) or Group 2 (G2) decoder yields significant performance improvements. Notably, G1 injection serves as the primary contributor, achieving superior accuracy compared to G2. We attribute this to

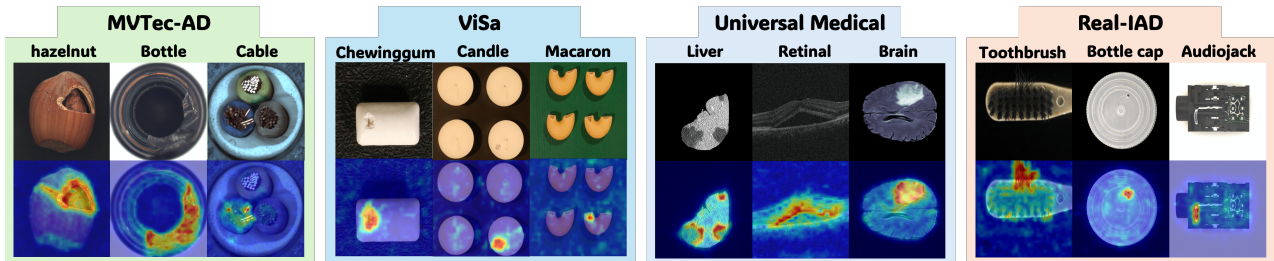


Figure 4. Qualitative results of our ShortcutBreaker on the MVTec-AD, ViSa, Universal Medical, and Real-IAD datasets. The first row displays the input images with their ground truth, while the second row presents the corresponding anomaly maps.

Table 2. Ablations studies of component contributions on Real-IAD and MvTec dataset, including LRNB: low-rank noisy bottleneck, FFB: frequency filtering block, GF: global filtering and GLM: global-local masking. (%)

LRNB	FFB		Real-IAD			MvTec-AD		
	GF	GLM	I-AUC/AP/F1	P-AUC/AP/F1/AUPRO		I-AUC/AP/F1	P-AUC/AP/F1/AUPRO	
	basemodel		84.7/81.3/75.8	97.6/32.7/39.8/91.4		98.6/99.1/97.8	97.3/61.7/62.9/93.0	
✓			88.7/86.6/79.5	98.5/40.7/46.4/93.5		99.7/99.8/99.4	98.4/70.1/69.8/94.9	
	✓		84.8/81.4/75.8	97.7/32.8/39.8/91.4		98.8/99.3/97.8	97.2/61.3/63.1/92.8	
	✓	✓	85.3/81.9/76.0	97.7/33.5/40.4/91.5		99.1/99.5/98.3	97.3/62.1/63.4/93.0	
✓	✓		89.6/86.5/80.4	98.8/46.3/48.9/94.4		99.6/99.8/99.1	98.2/69.7/69.1/94.8	
✓	✓	✓	<b>90.8/88.2/81.5</b>	<b>98.9/46.6/49.7/95.0</b>		<b>99.8/99.9/99.4</b>	<b>98.5/71.5/70.5/95.6</b>	

Table 3. Effect of dual injection in LRNB on Real-IAD, G1 and G2 denotes the injection of LRNB before group 1 and group 2 decoder. (%)

LRNB	I-AUC/AP/F1	P-AUC/AP/F1/AUPRO
None	85.3/81.9/76.9	97.7/33.4/30.4/91.5
G1	90.2/87.5/81.1	98.9/45.2/48.5/94.8
G2	88.7/86.0/79.3	98.0/45.6/49.1/94.0
G1+G2	<b>90.8/88.2/81.5</b>	<b>98.9/46.6/49.7/95.0</b>

Table 4. Effect of global and local masking in FFB on Real-IAD, GM: global masking, LM: local masking and GLM: global-local masking. (%)

FFB	I-AUC/AP/F1	P-AUC/AP/F1/AUPRO
None	89.6/86.5/80.4	98.8/46.3/48.9/94.4
GM	89.8/86.9/80.5	98.8/46.3/49.2/94.7
LM	90.0/86.8/80.6	99.0/46.4/49.2/94.7
GLM	<b>90.8/88.2/81.5</b>	<b>98.9/46.6/49.7/95.0</b>

the fact that G1 injection influences all subsequent decoder blocks, whereas G2 only affects the final four blocks. Furthermore, the combination of G1 and G2 surpasses single-injection strategies at both the image and pixel levels by further enlarging the score gap between normal and abnormal cases. The corresponding training loss and anomaly score plots in Fig. 3 corroborate these findings. Table 4 evaluates Global-Local Masking (GLM). While GM or LM alone yields marginal gains, combining them significantly boosts performance. This confirms our observation that

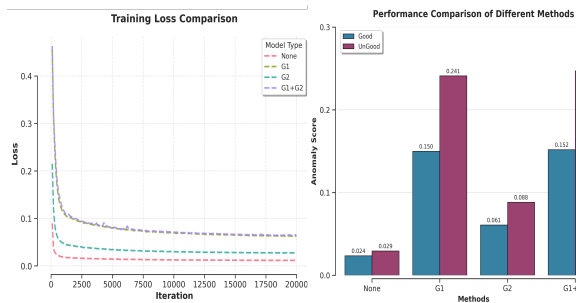


Figure 5. The corresponding plots of training loss (left part) and the averaged anomaly scores (right part) of the methods in Table 3.

ViT features suffer from information leakage via both self-identity and long-range token correlations, necessitating a dual-masking approach. The GLM prevents the shortcuts globally and locally, thus enhancing the anomaly detection ability.

**Comparison between LRNB and previous noisy bottlenecks** Previous methods also proposed some noisy operations in the bottleneck to avoid identity shortcuts, such as feature jittering (FJ) in UniAD (You et al., 2022) and noisy dropout bottleneck (NDB) in Dinomaly (Guo et al., 2025). To further validate the advantage of the proposed LRNB, we conduct a comparison in Table 5. The results in this table demonstrate that FJ experiences a performance drop and NDB yields slight improvements compared to models without such noise operations, while our LRNB and LRNB-D achieve a significant enhancement.

To explore the capacity of these operations in addressing

Table 5. Performance comparison of different bottlenecks (BNs) on Real-IAD. G1 denotes the bottleneck is only injected before group 1 decoder (%)

Bolltneack	I-AUC/AP/F1	P-/AUC/AP/F1/AUPRO
None	84.7/81.3/75.8	97.6/32.7/39.8/91.4
FJ (G1)	87.6/84.5/78.3	98.3/40.1/44.8/92.3
NBD (G1)	88.5/86.0/79.2	98.5/43.3/47.1/93.5
LRNB (G1)	90.2/87.5/81.1	98.9/45.2/48.5/94.8
LRNB (G1+G2)	<b>90.8/88.2/81.5</b>	<b>98.9/46.6/49.7/95.0</b>

Table 7. Comparison of computational cost of different methods on Real-IAD, mAD is the average value of all the metrics. Shortcutbreaker-s is based on the encoder of ViT-small model, Shortcutbreaker-s\* is based on ViT-small model and trained with 224x224 images.

Method	Params(M)	FLOPS(G)	mAD (%)
UniAD	<b>24.5</b>	<b>3.6</b>	67.5
DiAD	1331.3	451.5	52.6
MambaAD	<u>25.7</u>	8.3	72.7
Dinomaly	132.8	104.7	77.0
<b>Shortcutbreaker</b>	109.8	86.5	<b>78.7</b>
<b>Shortcutbreaker-s</b>	27.6	21.8	<u>77.5</u>
<b>Shortcutbreaker-s*</b>	27.6	<u>7.19</u>	73.3

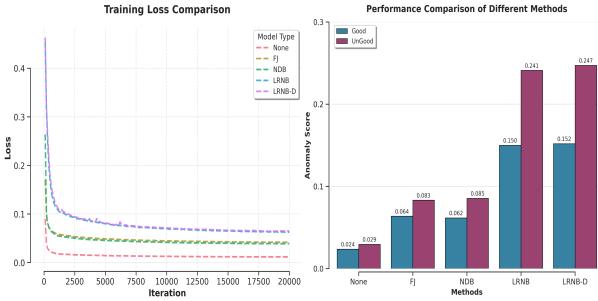


Figure 6. The plots of training loss (left part) and the averaged anomaly scores (right part) of different bottlenecks on Real-IAD. the "identity mapping" issue, we further examine the corresponding training loss and average anomaly score. As shown in Fig. 6, models without a bottleneck achieve near-zero training loss and obtain extremely close anomaly scores between normal and abnormal cases (0.024 vs. 0.029). These results indicate that these models suffer from identity mapping behavior where inputs are directly replicated in outputs. Introducing FJ or NDB noise operations partially alleviates this issue, which we attribute to enhanced noise robustness from exposure to diverse industrial patterns. Our LRNB and LRNB-D effectively resolve identity mapping: while moderately increasing the score of normal data, it substantially enhances the score of abnormal cases. This strategic trade-off widens the discrimination margin between normal and abnormal samples, ultimately improving anomaly detection performance. **Comparison between FFB and previous modules in decoder** Prior works have introduced specialized decoder modules to mitigate iden-

Table 6. Performance comparison of different modules in decoder on Real-IAD. (%)

Decoder Blocks	I-AUC/AP/F1	P-/AUC/AP/F1/AUPRO
ViT	88.7/86.6/79.5	98.5/40.7/46.4/93.5
CNN+ViT	89.0/86.1/79.5	98.8/45.5/48.7/94.4
NMA+ViT	90.4/88.0/81.2	98.9/45.4/48.9/94.6
LSA	89.3/87.5/79.9	98.6/43.4/47.9/93.9
FFB (ours)	<b>90.8/88.2/81.5</b>	<b>98.9/46.6/49.7/95.0</b>

tity mapping. For instance, (Lu et al., 2024) attributes this issue to encoder-decoder homogeneity and advocates for heterogeneous structures, such as using CNN blocks to reconstruct ViT encoder outputs. Similarly, (You et al., 2022) introduced neighbor-masking attention (NMA) to prevent information leakage, while (Guo et al., 2025) utilized linear self-attention (LSA) to "un-focus" features for robust reconstruction. As shown in Table 6, replacing the ViT baseline with a hybrid ViT+CNN structure improves performance, with LSA providing further gains. Additionally, NMA proves effective in the ViT decoder, yielding improvements of 0.7/1.4/1.7 in image-level and 0.1/4.7/2.5/1.0 in pixel-level metrics over pure ViT with negligible computational overhead. Ultimately, our FFB outperforms all existing methods across all metrics, which we attribute to its superior adaptability to ViT-extracted tokens.

**Comparison of computational complexity** Table ?? presents the trade-off between computational complexity and mAD on Real-IAD dataset. where our Shortcutbreaker framework demonstrates clear superiority over state-of-the-art methods. Notably, the primary Shortcutbreaker variant achieves a peak performance of 78.7 mAD, surpassing the second-best Dinomaly while reducing computational costs by 17.4%. Furthermore, Shortcutbreaker-S and Shortcutbreaker-S\* offer exceptional scalability; the former maintains a superior 77.5 mAD with only 27.6M parameters, while the latter delivers a highly efficient 7.19G FLOPs for real-time applications, even better than the light-weight structure of MambaAD (He et al., 2024a).

## 4. Conclusion

We propose ShortcutBreaker, a novel feature-reconstruction framework designed to mitigate identity shortcuts in the MUAD setting. It introduces two core innovations: a low-rank noisy bottleneck (LRNB) and a frequency-filtering block (FFB), which prevent shortcut learning within the bottleneck and decoder components. Extensive experiments across four well-established benchmarks confirm the efficacy of these modules, demonstrating consistent superiority over state-of-the-art methods, particularly in diverse scenarios. Furthermore, its low GFLOPs underline its potential for real-time applications.

## Impact Statement

This paper presents work whose goal is to advance the field of Machine Learning. There are many potential societal consequences of our work, none of which we feel must be specifically highlighted here.

## References

- Angiulli, F., Basta, S., and Pizzuti, C. Distance-based detection and prediction of outliers. *IEEE transactions on knowledge and data engineering*, 18(2):145–160, 2005.
- Bergmann, P., Fauser, M., Sattlegger, D., and Steger, C. Mvtec ad—a comprehensive real-world dataset for unsupervised anomaly detection. In *Proceedings of the IEEE/CVF conference on computer vision and pattern recognition*, pp. 9592–9600, 2019.
- Breunig, M. M., Kriegel, H.-P., Ng, R. T., and Sander, J. Lof: identifying density-based local outliers. In *Proceedings of the 2000 ACM SIGMOD international conference on Management of data*, pp. 93–104, 2000.
- Cai, Y., Chen, H., and Cheng, K.-T. Rethinking autoencoders for medical anomaly detection from a theoretical perspective. In *International Conference on Medical Image Computing and Computer-Assisted Intervention*, pp. 544–554. Springer, 2024.
- Darcet, T., Oquab, M., Mairal, J., and Bojanowski, P. Vision transformers need registers. *arXiv preprint arXiv:2309.16588*, 2023.
- Defard, T., Setkov, A., Loesch, A., and Audigier, R. Padim: a patch distribution modeling framework for anomaly detection and localization. In *International Conference on Pattern Recognition*, pp. 475–489. Springer, 2021.
- Deng, H. and Li, X. Anomaly detection via reverse distillation from one-class embedding. In *Proceedings of the IEEE/CVF conference on computer vision and pattern recognition*, pp. 9737–9746, 2022.
- Deng, J., Dong, W., Socher, R., Li, L.-J., Li, K., and Fei-Fei, L. Imagenet: A large-scale hierarchical image database. In *2009 IEEE conference on computer vision and pattern recognition*, pp. 248–255. Ieee, 2009.
- Goodfellow, I., Bengio, Y., Courville, A., and Bengio, Y. *Deep learning*, volume 1. MIT press Cambridge, 2016.
- Guan, H., Li, Q., Yan, Z., and Wei, W. Slof: identify density-based local outliers in big data. In *2015 12th Web Information System and Application Conference (WISA)*, pp. 61–66. IEEE, 2015.
- Guo, J., Lu, S., Jia, L., Zhang, W., and Li, H. Encoder-decoder contrast for unsupervised anomaly detection in medical images. *IEEE Transactions on Medical Imaging*, 2023.
- Guo, J., Jia, L., Zhang, W., Li, H., et al. Recontrast: Domain-specific anomaly detection via contrastive reconstruction. *Advances in Neural Information Processing Systems*, 36, 2024.
- Guo, J., Lu, S., Zhang, W., Chen, F., Li, H., and Liao, H. Dinomaly: The less is more philosophy in multi-class unsupervised anomaly detection. In *Proceedings of the Computer Vision and Pattern Recognition Conference*, pp. 20405–20415, 2025.
- He, H., Bai, Y., Zhang, J., He, Q., Chen, H., Gan, Z., Wang, C., Li, X., Tian, G., and Xie, L. Mambaad: Exploring state space models for multi-class unsupervised anomaly detection. *Advances in Neural Information Processing Systems*, 37:71162–71187, 2024a.
- He, H., Zhang, J., Chen, H., Chen, X., Li, Z., Chen, X., Wang, Y., Wang, C., and Xie, L. A diffusion-based framework for multi-class anomaly detection. In *Proceedings of the AAAI Conference on Artificial Intelligence*, volume 38, pp. 8472–8480, 2024b.
- He, K., Zhang, X., Ren, S., and Sun, J. Deep residual learning for image recognition. In *Proceedings of the IEEE conference on computer vision and pattern recognition*, pp. 770–778, 2016.
- He, K., Chen, X., Xie, S., Li, Y., Dollár, P., and Girshick, R. Masked autoencoders are scalable vision learners. In *Proceedings of the IEEE/CVF conference on computer vision and pattern recognition*, pp. 16000–16009, 2022.
- He, L., Jiang, Z., Peng, J., Zhu, W., Liu, L., Du, Q., Hu, X., Chi, M., Wang, Y., and Wang, C. Learning unified reference representation for unsupervised multi-class anomaly detection. In *European Conference on Computer Vision*, pp. 216–232. Springer, 2024c.
- Hido, S., Tsuboi, Y., Kashima, H., Sugiyama, M., and Kanamori, T. Statistical outlier detection using direct density ratio estimation. *Knowledge and information systems*, 26:309–336, 2011.
- Hu, E. J., Shen, Y., Wallis, P., Allen-Zhu, Z., Li, Y., Wang, S., Wang, L., Chen, W., et al. Lora: Low-rank adaptation of large language models. *ICLR*, 1(2):3, 2022.
- Knorr, E. M., Ng, R. T., and Tucakov, V. Distance-based outliers: algorithms and applications. *The VLDB Journal*, 8(3):237–253, 2000.

- Li, C.-L., Sohn, K., Yoon, J., and Pfister, T. Cutpaste: Self-supervised learning for anomaly detection and localization. In *Proceedings of the IEEE/CVF conference on computer vision and pattern recognition*, pp. 9664–9674, 2021.
- Liu, Z., Zhou, Y., Xu, Y., and Wang, Z. Simplenet: A simple network for image anomaly detection and localization. In *Proceedings of the IEEE/CVF Conference on Computer Vision and Pattern Recognition*, pp. 20402–20411, 2023.
- Loshchilov, I. and Hutter, F. Sgdr: Stochastic gradient descent with warm restarts. *arXiv preprint arXiv:1608.03983*, 2016.
- Lu, S., Zhang, W., Zhao, H., Liu, H., Wang, N., and Li, H. Anomaly detection for medical images using heterogeneous auto-encoder. *IEEE Transactions on Image Processing*, 2024.
- Reddi, S. J., Kale, S., and Kumar, S. On the convergence of adam and beyond. *arXiv preprint arXiv:1904.09237*, 2019.
- Roth, K., Pemula, L., Zepeda, J., Schölkopf, B., Brox, T., and Gehler, P. Towards total recall in industrial anomaly detection. In *Proceedings of the IEEE/CVF conference on computer vision and pattern recognition*, pp. 14318–14328, 2022.
- Rousseeuw, P. J. and Hubert, M. Robust statistics for outlier detection. *Wiley interdisciplinary reviews: Data mining and knowledge discovery*, 1(1):73–79, 2011.
- Tien, T. D., Nguyen, A. T., Tran, N. H., Huy, T. D., Duong, S., Nguyen, C. D. T., and Truong, S. Q. Revisiting reverse distillation for anomaly detection. In *Proceedings of the IEEE/CVF conference on computer vision and pattern recognition*, pp. 24511–24520, 2023.
- Van der Maaten, L. and Hinton, G. Visualizing data using t-sne. *Journal of machine learning research*, 9(11), 2008.
- Wang, C., Zhu, W., Gao, B.-B., Gan, Z., Zhang, J., Gu, Z., Qian, S., Chen, M., and Ma, L. Real-iad: A real-world multi-view dataset for benchmarking versatile industrial anomaly detection. In *Proceedings of the IEEE/CVF Conference on Computer Vision and Pattern Recognition*, pp. 22883–22892, 2024.
- Wortsman, M., Dettmers, T., Zettlemoyer, L., Morcos, A., Farhadi, A., and Schmidt, L. Stable and low-precision training for large-scale vision-language models. *Advances in Neural Information Processing Systems*, 36: 10271–10298, 2023.
- Yi, J. and Yoon, S. Patch svdd: Patch-level svdd for anomaly detection and segmentation. In *Proceedings of the Asian conference on computer vision*, 2020.
- Yin, H., Jiao, G., Wu, Q., Karlsson, B. F., Huang, B., and Lin, C. Y. Lafite: Latent diffusion model with feature editing for unsupervised multi-class anomaly detection. *arXiv preprint arXiv:2307.08059*, 2023.
- You, Z., Cui, L., Shen, Y., Yang, K., Lu, X., Zheng, Y., and Le, X. A unified model for multi-class anomaly detection. *Advances in Neural Information Processing Systems*, 35: 4571–4584, 2022.
- Zavrtanik, V., Kristan, M., and Skočaj, D. Draem-a discriminatively trained reconstruction embedding for surface anomaly detection. In *Proceedings of the IEEE/CVF international conference on computer vision*, pp. 8330–8339, 2021.
- Zhang, J., Chen, X., Wang, Y., Wang, C., Liu, Y., Li, X., Yang, M.-H., and Tao, D. Exploring plain vit reconstruction for multi-class unsupervised anomaly detection. *arXiv preprint arXiv:2312.07495*, 2023.
- Zhang, J., Wang, C., Li, X., Tian, G., Xue, Z., Liu, Y., Pang, G., and Tao, D. Learning feature inversion for multi-class anomaly detection under general-purpose coco-ad benchmark. *arXiv preprint arXiv:2404.10760*, 2024.
- Zhang, R., Isola, P., Efros, A. A., Shechtman, E., and Wang, O. The unreasonable effectiveness of deep features as a perceptual metric. In *Proceedings of the IEEE conference on computer vision and pattern recognition*, pp. 586–595, 2018.
- Zhao, Y. Omnia: A unified cnn framework for unsupervised anomaly localization. In *Proceedings of the IEEE/CVF Conference on Computer Vision and Pattern Recognition*, pp. 3924–3933, 2023.
- Zhao, Y., Ding, Q., and Zhang, X. Ae-flow: Autoencoders with normalizing flows for medical images anomaly detection. In *The Eleventh International Conference on Learning Representations*, 2023.
- Zou, Y., Jeong, J., Pemula, L., Zhang, D., and Dabeer, O. Spot-the-difference self-supervised pre-training for anomaly detection and segmentation. In *European Conference on Computer Vision*, pp. 392–408. Springer, 2022.

## A. Appendix

### A.1. Proofs

In this section, we will provide the proof of the first property of low-rank matrix decomposition under non-linear transformation, the analysis of rank constraints of the proposition 1 in (Cai et al., 2024). In our proofs, we assume the input feature matrix  $x \in \mathbb{R}^d$  maintains full column rank. This assumption aligns with our empirical observations from practical computations using Singular Value Decomposition (SVD).

**Analysis of rank constraints of the proposition 1 in (Cai et al., 2024)** Given the condition of linear transformation, Proposition 1 in (Cai et al., 2024) establishes that for  $k \geq \frac{d}{2}$ , the  $W_1 W_2 = I_{d \times d}$  with  $W_1 \in \mathbb{R}^{d \times k}$  and  $W_2 \in \mathbb{R}^{k \times d}$  admits at least one solution. Consequently, in turns, when no solutions exist for this equation,  $k < \frac{d}{2}$ , thereby inherently suppressing identity mapping. However, a critical paradox emerges in the transitional regime  $d > k \geq \frac{d}{2}$ : Proposition 1 guarantees solution existence, but the rank inequality  $r(W_1 W_2) \leq \min(r(W_1), r(W_2)) \leq k < d$  directly conflicts with the full-rank requirement  $I_{d \times d} = d$ . Therefore, this reasoning process is flawed.

Table 8. Effect of dual injection in LRNB on Real-IAD and MvTec-AD, G1 and G2 denotes the injection of LRNB before group 1 and group 2 decoder.

LRNB	Real-IAD		MvTec-AD	
	I-AUC/AP/F1	P-/AUC/AP/F1/AUPRO	I-AUC/AP/F1	P-/AUC/AP/F1/AUPRO
None	84.7/81.3/75.8	97.6/32.7/39.8/91.4	99.1/99.5/98.3	97.3/62.1/63.4/93.0
G1	90.2/87.5/81.1	98.9/45.2/48.5/94.8	99.8/99.9/99.4	98.4/70.5/69.7/95.5
G2	88.7/86.0/79.3	98.0/45.6/49.1/94.0	99.4/99.7/98.9	97.9/70.3/69.2/94.5
G1+G2	<b>90.8/88.2/81.5</b>	<b>98.9/46.6/49.7/95.0</b>	<b>99.8/99.9/99.4</b>	<b>98.5/71.5/70.5/95.6</b>

Table 9. Performance comparison of different bottlenecks on Real-IAD and MvTec-AD datasets. G1 denotes the bottleneck is only injected before group 1 decoder (%)

Bottleneck	Real-IAD		MvTec-AD	
	I-AUC/AP/F1	P-/AUC/AP/F1/AUPRO	I-AUC/AP/F1	P-/AUC/AP/F1/AUPRO
None	84.7/81.3/75.8	97.6/32.7/39.8/91.4	99.1/99.5/98.3	97.3/62.1/63.4/93.0
FJ (G1)	87.6/84.5/78.3	98.3/40.1/44.8/92.3	99.5/99.7/98.9	98.1/68.2/68.0/94.5
NBD (G1)	88.5/86.0/79.2	98.5/43.3/47.1/93.5	99.7/99.8/99.1	98.2/68.8/68.7/94.8
LRNB (G1)	90.2/87.5/81.1	98.9/45.2/48.5/94.8	99.8/99.9/99.4	98.4/70.5/69.7/95.5
LRNB((G1+G2))	<b>90.8/88.2/81.5</b>	<b>98.9/46.6/49.7/95.0</b>	<b>99.8/99.9/99.4</b>	<b>98.5/71.5/70.5/95.6</b>

Table 10. Performance comparison of different modules in decoder on Real-IAD and MvTec-AD dataset. (%)

Decoder	Real-IAD		MvTec-AD	
	I-AUC/AP/F1	P-/AUC/AP/F1/AUPRO	I-AUC/AP/F1	P-/AUC/AP/F1/AUPRO
ViT	88.7/86.6/79.5	98.5/40.7/46.4/93.5	99.7/99.8/99.4	98.4/70.1/69.8/94.9
CNN+ViT	89.0/86.1/79.5	98.8/45.5/48.7/94.4	99.7/99.8/99.4	98.3/70.1/69.8/94.9
NMA+ViT	90.4/88.0/81.2	98.9/45.4/48.9/94.6	99.7/99.9/99.4	98.4/71.2/69.9/95.1
LA	89.3/87.5/79.9	98.6/43.4/47.9/93.9	99.2/99.7/98.9	97.5/62.5/64.8/92.6
FFB (Ours)	<b>90.8/88.2/81.5</b>	<b>98.9/46.6/49.7/95.0</b>	<b>99.8/99.9/99.4</b>	<b>98.5/71.5/70.5/95.6</b>

### A.2. Supplementary Ablation Studies

Due to the page limit of main text, we present more ablation studies in this section of Appendix.

Table 8 extends Table 3 to the MvTec-AD dataset, confirming the efficacy of the dual injection strategy. Observations remain consistent: although both G1 and G2 injections improve performance, G1 provides the most significant gain. Crucially, the G1 and G2 combination outperforms either standalone injection.

Table 11. The effect of dropout rate in LRNB. (%)

LRNB nosie rate	Real-IAD		MvTec-AD	
	I-AUC/AP/F1	P-/AUC/AP/F1/AUPRO	I-AUC/AP/F1	P-/AUC/AP/F1/AUPRO
0	89.5/86.6/80.0	98.9/45.2/48.1/94/1	99.5/99.7/98.7	98.1/67.2/67.0/94.2
0.1	89.9/87.1/80.7	98.9/46.0/49.0/94.5	99.6/99.7/99.1	98.4/70.6/69.7/94.9
0.2	90.2/87.4/80.9	98.9/46.8/49.2/94.7	99.7/99.8/99.2	98.5/71.3/70.2/95.3
0.3	90.3/87.5/81.0	98.9/46.0/49.2/94.8	99.7/99.9/99.4	98.5/71.2/70.2/95.4
0.4	<b>90.8/88.2/81.5</b>	<b>98.9/46.6/49.7/95.0</b>	<b>99.8/99.9/99.4</b>	<b>98.5/71.5/70.5/95.6</b>
0.5	90.6/88.0/81.5	99.0/45.9/49.1/94.9	99.7/99.9/99.4	98.5/71.5/70.5/95.7

Table 12. The effect of layer number in LRNB. (%)

Layer number $i$	Real-IAD		MvTec-AD	
	I-AUC/AP/F1	P-/AUC/AP/F1/AUPRO	I-AUC/AP/F1	P-/AUC/AP/F1/AUPRO
1	89.4/87.1/80.2	98.7/46.2/48.9/94.0	<b>99.8/99.9/99.4</b>	<b>98.5/71.5/70.5/95.6</b>
2	<b>90.8/88.2/81.5</b>	<b>98.9/46.6/49.7/95.0</b>	99.7/99.9/99.4	98.1/67.8/66.9/94.5
3	90.3/87.6/81.1	99.0/45.2/48.8/94.8	99.5/99.9/99.2	97.6/59.9/61.1/92.7

Extending Table 5 to MVTec-AD, Table 10 validates our FFB. Compared to FJ and NDB, LRNB achieves substantial gains across both datasets. Specifically, incorporating dual injection strategy in LRNB further enhances results by effectively enlarging the score margin between normal and abnormal cases.

Table 10 extends Table 6 to the MVTec-AD dataset, confirming the efficacy of our FFB. The results display that compared FJ and NDB, our LRNB significantly improve the performances on both datasets, further injection before G2 further improve the performance by widening the gap between normal and abnormal samples.

Table 13. The effect of low-rank ratio  $r$  in LRNB. (%)

low-rank ratio $r$	Real-IAD		MvTec-AD	
	I-AUC/AP/F1	P-/AUC/AP/F1/AUPRO	I-AUC/AP/F1	P-/AUC/AP/F1/AUPRO
2	89.9/87.2/80.5	98.9/46.5/49.0/94.4	99.7/99.8/99.3	98.3/70.8/70.0/95.3
4	<b>90.8/88.2/81.5</b>	<b>98.9/46.6/49.7/95.0</b>	<b>99.8/99.9/99.4</b>	<b>98.5/71.5/70.5/95.6</b>
6	89.7/86.6/80.3	98.8/44.7/48.2/84.6	99.7/99.8/99.3	98.4/71.4/70.4/95.6
8	90.0/87.1/80.7	99.0/45.5/48.7/94.8	99.3/99.7/98.8	98.0/66.0/66.6/94.1
10	90.0/87.2/80.5	98.9/45.0/47.8/94.4	99.8/99.9/99.4	98.4/70.6/70.1/95.8

### A.3. Hyperparameter Analysis

In this section, we will present the experiments about the hyper-parameter selection and analysis, which are divided into two parts: LRNB related hyperparameter and FFU related hyperparameter.

**LRNB:** First, we investigate the hyper-parameter settings for LRNB, specifically the impact of dropout. Integrated to perturb tokens and mitigate identity mapping, this mechanism improves performance across the 0.1–0.5 range compared to the baseline (dropout=0.0), as shown in Table 11, with 0.4 yielding the best results. Second, we explore the effect of different LRNB layer number ( $i$ ) in Table A.2. Observations indicate the optimal setting is  $i = 1$  for MVTec-AD and  $i = 2$  for Real-IAD. This difference is attributed to varying dataset complexity; the more diverse Real-IAD dataset requires stronger noise perturbation to suppress identity shortcuts. Following Dinomaly (Guo et al., 2025), we set  $i = 1$  for MVTec-AD and VisA, and  $i = 2$  for Real-IAD and Universal Medical datasets. Third, we investigate the impact of dropout noise within the downsampling and upsampling blocks (DBs and UBs). As shown in Table 14, the best performance is achieved when dropout operations are embedded solely in the UBs. Forth, Table 13 evaluates the impact of varying the LRNB low-rank ratio  $r$ , where a lower  $r$  indicates more intense token perturbation. Optimal performance is achieved at  $r = 4$ , suggesting that excessive perturbation can hinder the reconstruction of normal samples. Consequently, a balanced  $r$  is essential to maximize the discriminative gap between normal and abnormal samples while preserving the reconstruction integrity of

Table 14. The effect of noise operation in downsampling blocoks (DBs) and upsamling blocks (UBs) of LRNB. (%)

UB	DB	Real-IAD		MvTec-AD	
		I-AUC/AP/F1	P-/AUC/AP/F1/AUPRO	I-AUC/AP/F1	P-/AUC/AP/F1/AUPRO
	✓	90.3/87.6/81.0	99.1/48.3/50.2/94.8	99.7/99.8/99.2	98.4/70.9/70.2/95.0
✓		<b>90.8/88.2/81.5</b>	<b>98.9/46.6/49.7/95.0</b>	<b>99.8/99.9/99.4</b>	<b>98.5/71.5/70.5/95.6</b>
✓	✓	90.2/87.5/81.0	98.9/47.4/49.7/95/0	99.8/99.9/99.4	98.5/71.2/70.2/95.6

Table 15. The effect of noise ratio in global masking (dropout operation on frequency-spectral filter  $W_{freq}$ ) of FFU. (%)

noise ratio in GM	Real-IAD		MvTec-AD	
	I-AUC/AP/F1	P-/AUC/AP/F1/AUPRO	I-AUC/AP/F1	P-/AUC/AP/F1/AUPRO
0	89.6/86.5/80.4	98.8/46.3/48.9/94.4	99.7/99.8/99.4	98.4/71.0/70.2/95.3
0.1	90.2/87.2/81.1	98.8/46.0/49.3/94.8	99.7/99.9/99.4	98.5/71.3/70.5/95.4
0.2	90.5/87.9/81.4	98.9/46.1/49.5/94.9	99.7/99.9/99.4	98.4/71.2/70.4/95.5
0.3	<b>90.8/88.2/81.5</b>	<b>98.9/46.6/49.7/95.0</b>	<b>99.8/99.9/99.4</b>	<b>98.5/71.5/70.5/95.6</b>
0.4	90.3/87.6/81.0	98.8/46.9/49.9/94.8	99.8/99.9/99.4	<b>98.5/71.5/70.5/95.7</b>
0.5	90.4/87.8/81.2	98.9/45.7/49.1/94.8	99.8/99.9/99.4	98.5/71.5/70.4/95.6

normal patterns.

**FFU:** In this part, we explore the hyper-parameter setting for FFU. First, we investigate the impact of the Global Masking (GM) ratio (dropout on the spectral filter  $W_{freq}$ ) in Table 15. The results demonstrate that GM consistently enhances performance, confirming its robustness, with an optimal noise ratio of 0.3. Second, we explore the influence of the mask size of Local Masking (LM) in Table 16. The results indicate that the LM mechanism consistently improves performance compared to the baseline without local masking. The highest accuracy is achieved with a mask size of 5 across both datasets, further validating the effectiveness of local frequency-domain perturbation.

#### A.4. Detailed Results

We further display the detailed quantitative results on four benchmarks, i.e., MvTec-AD (Bergmann et al., 2019), ViSA (Zou et al., 2022), Universal Medical (He et al., 2024b) and Real-IAD (Wang et al., 2024) in Table 17-20, respectively. Also, we display the visualized results of our method on above four datasets in Fig. 7-10, respectively.

Table 16. The effect of mask size in local masking (center zero operation on frequency-spectral filter  $W_{freq}$ ) of FFU. (%)

noise ratio in GM	Real-IAD		MvTec-AD	
	I-AUC/AP/F1	P-/AUC/AP/F1/AUPRO	I-AUC/AP/F1	P-/AUC/AP/F1/AUPRO
None	89.6/86.5/80.4	98.8/46.3/48.9/94.4	99.6/99.8/99.1	98.2/69.7/69.1/94.8
3	90.3/87.5/80.9	98.9/46.6/49.7/94.9	99.7/99.8/99.4	98.4/70.7/70.1/95.0
5	<b>90.8/88.2/81.5</b>	<b>98.9/46.6/49.7/95.0</b>	<b>99.8/99.9/99.4</b>	<b>98.5/71.5/70.5/95.6</b>
7	90.3/87.5/81.0	98.9/46.2/49.3/94.8	99.7/99.8/99.4	98.4/71.5/70.4/95.6
9	89.9/87.1/80.7	99.0/46.5/49.2/94.5	99.7/99.9/99.4	98.4/71.8/70.6/95.8

Table 17. Detailed quantitative results on MvTec-AD (Bergmann et al., 2019). Good score means the averaged anomaly score of normal data in this class, UnGood score indicates that of abnormal data. (%)

Class	I-Auroc/I-AP/I-F1	P-AUROC/P-AP/P-F1/P-AUPRO	Good Score	UnGood Score
carpet	99.4/99.8/99.4	99.3/71.6/72.6/97.6	0.1007	0.2806
grid	99.9/100.0/99.1	99.5/63.6/62.9/97.7	0.0784	0.3184
leather	100.0/100.0/100.0	99.4/53.2/55.7/98.0	0.0795	0.2703
tile	100.0/100.0/100.0	97.8/73.8/74.7/88.5	0.0976	0.3215
wood	99.9/100.0/99.2	97.7/73.7/70.0/94.2	0.1092	0.3011
bottle	100.0/100.0/100.0	99.2/89.0/84.3/97.0	0.0902	0.3085
cable	100.0/100.0/99.5	98.9/79.9/77.9/94.7	0.1169	0.2498
capsule	98.4/99.7/98.6	98.7/63.5/61.2/97.5	0.0825	0.1764
hazelnut	100.0/100.0/100.0	99.5/83.6/77.7/97.2	0.1018	0.2503
metal_nut	100.0/100.0/100.0	97.0/79.7/86.3/94.8	0.1052	0.2711
pill	99.7/99.9/98.9	97.8/76.1/71.3/97.8	0.0831	0.1682
screw	99.5/99.8/97.9	99.7/65.0/62.1/98.7	0.0875	0.1494
toothbrush	100.0/100.0/100.0	99.1/58.9/65.4/95.8	0.1115	0.2779
transistor	99.5/99.2/98.8	94.3/60.9/59.2/88.0	0.108	0.23
zipper	100.0/100.0/100.0	99.2/80.5/76.1/97.0	0.0731	0.2373
Mean	99.8/99.9/99.4	98.5/71.5/70.5/95.6	0.095	0.254

Table 18. Detailed quantitative results on VisA (Zou et al., 2022). Good score means the averaged anomaly score of normal data in this class, UnGood score indicates that of abnormal data. (%)

Class	I-Auroc/I-AP/I-F1	P-AUROC/P-AP/P-F1/P-AUPRO	Good Score	UnGood Score
candle	98.2/98.3/93.5	99.4/46.3/49.4/94.9	0.0646	0.1215
capsules	98.9/99.2/96.9	99.6/67.9/67.5/97.8	0.0796	0.1632
cashew	98.4/99.3/96.5	97.5/67.6/63.9/92.2	0.0846	0.1387
chewinggum	99.7/99.9/98.5	99.1/70.5/68.2/87.0	0.0894	0.2015
fryum	98.7/99.4/96.0	97.0/52.5/54.4/93.7	0.0774	0.164
macaroni1	97.8/97.7/92.5	99.5/34.8/40.9/96.0	0.0602	0.0956
macaroni2	95.6/95.4/89.5	99.7/25.3/37.2/98.6	0.0662	0.0894
pcb1	99.1/99.1/97.1	99.7/88.0/79.5/96.1	0.0833	0.1827
pcb2	99.2/99.0/97.5	99.1/29.7/37.3/92.8	0.0933	0.187
pcb3	99.3/99.3/96.5	99.0/42.2/41.3/94.7	0.0863	0.1801
pcb4	99.9/99.9/98.0	98.9/60.4/55.3/94.8	0.0827	0.2233
pipe_fryum	98.9/99.5/96.4	99.2/61.7/65.4/95.3	0.0787	0.1623
Mean	98.7/98.8/95.8	99.0/53.9/55.0/94.5	0.0789	0.1591

**ShortcutBreaker: Low-Rank Noisy Bottleneck and Frequency Filtering Block for Multi-Class Unsupervised Anomaly Detection**

Table 19. Detailed quantitative results on Universal Medical (He et al., 2024b). Good score means the averaged anomaly score of normal data in this class, UnGood score indicates that of abnormal data. (%)

Class	I-Auroc/I-AP/I-F1	P-AUROC/P-AP/P-F1/P-AUPRO	Good Score	UnGood Score
brain	95.6/99.0/95.0	98.0/69.2/68.3/84.5	0.2305	0.3586
liver	73.1/68.9/67.0	97.5/27.1/33.9/93.5	0.198	0.2494
retinal	94.2/93.0/85.5	95.9/71.7/64.7/84.0	0.1751	0.2837
Mean	87.6/87.0/82.5	97.1/56.0/55.6/87.3	0.2012	0.2972

Table 20. Detailed quantitative results on Real-IAD (Wang et al., 2024). Good score means the averaged anomaly score of normal data in this class, UnGood score indicates that of abnormal data. (%)

Class	I-Auroc/I-AP/I-F1	P-AUROC/P-AP/P-F1/P-AUPRO	Good Score	UnGood Score
audiojack	90.2/86.1/76.0	99.3/51.3/53.8/95.4	0.1915	0.2997
bottle_cap	90.5/88.2/80.5	99.7/38.9/40.4/98.0	0.1167	0.2108
button_battery	89.3/91.3/84.0	99.2/60.9/60.5/93.9	0.1605	0.2796
end_cap	86.9/86.5/84.2	99.0/20.1/31.0/95.8	0.165	0.217
eraser	93.5/91.6/82.3	99.7/47.8/51.2/98.1	0.141	0.2251
fire_hood	84.6/76.9/70.6	99.4/41.2/45.3/94.8	0.167	0.234
mint	78.5/78.2/70.4	97.8/31.9/40.4/82.2	0.1518	0.1937
mounts	87.2/76.3/76.2	99.5/43.7/45.7/95.2	0.1592	0.2511
pcb	93.5/95.9/89.0	99.4/60.3/59.9/96.1	0.1514	0.2496
phone_battery	93.5/91.6/84.2	95.9/43.5/48.8/97.2	0.166	0.289
plastic_nut	89.8/83.6/75.8	99.7/42.3/47.0/97.8	0.1313	0.204
plastic_plug	89.4/86.2/75.8	99.2/30.4/37.1/95.4	0.1446	0.2088
porcelain_doll	87.1/78.2/71.5	99.2/37.5/42.4/95.8	0.1317	0.1858
regulator	84.2/74.7/64.0	99.3/41.5/48.2/95.8	0.1294	0.1827
rolled_strip_base	99.0/99.5/96.7	99.8/49.7/50.4/98.6	0.1235	0.2445
sim_card_set	96.2/96.4/90.3	99.2/57.6/57.0/93.6	0.1405	0.2615
switch	97.9/98.3/93.3	97.3/70.8/66.7/96.3	0.1314	0.2695
tape	97.0/95.1/89.3	99.8/56.0/56.7/98.9	0.1154	0.2409
terminalblock	98.4/98.9/94.9	99.9/54.9/55.5/99.1	0.1225	0.2376
toothbrush	90.3/92.0/83.3	97.1/38.9/44.7/90.4	0.1802	0.2833
toy	88.6/91.1/84.6	96.5/27.3/34.1/93.3	0.1703	0.2312
toy_brick	80.7/76.7/69.2	97.6/32.2/39.4/83.8	0.2232	0.2818
transistor1	97.0/97.9/92.5	99.5/54.7/54.2/97.6	0.1453	0.2863
usb	95.1/94.6/87.9	99.5/49.2/51.6/98.1	0.1456	0.2786
usb_adaptor	85.1/78.5/72.4	99.2/28.1/37.5/94.2	0.1352	0.1853
u_block	92.8/89.1/79.1	99.6/49.9/55.6/97.1	0.133	0.2178
vcpill	93.0/92.7/84.2	99.2/73.9/70.0/94.9	0.1607	0.2727
wooden_beads	89.0/87.5/79.0	99.2/52.2/53.6/92.6	0.1695	0.2397
woodstick	84.9/74.6/67.5	99.2/52.2/54.3/92.3	0.2143	0.3009
zipper	99.0/99.5/96.4	99.0/57.9/59.2/96.5	0.139	0.3556
Mean	90.8/88.2/81.5	98.9/46.6/49.7/95.0	0.1519	0.2473

# ShortcutBreaker: Low-Rank Noisy Bottleneck and Frequency Filtering Block for Multi-Class Unsupervised Anomaly Detection

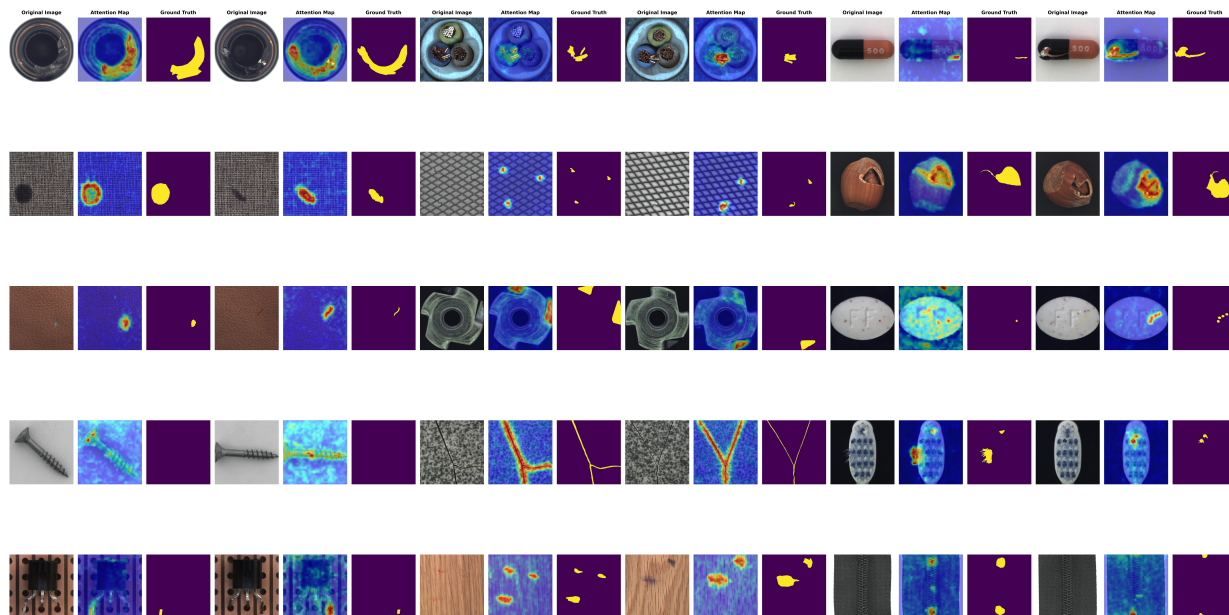


Figure 7. Qualitative results of our method on MVTec-AD (Bergmann et al., 2019).

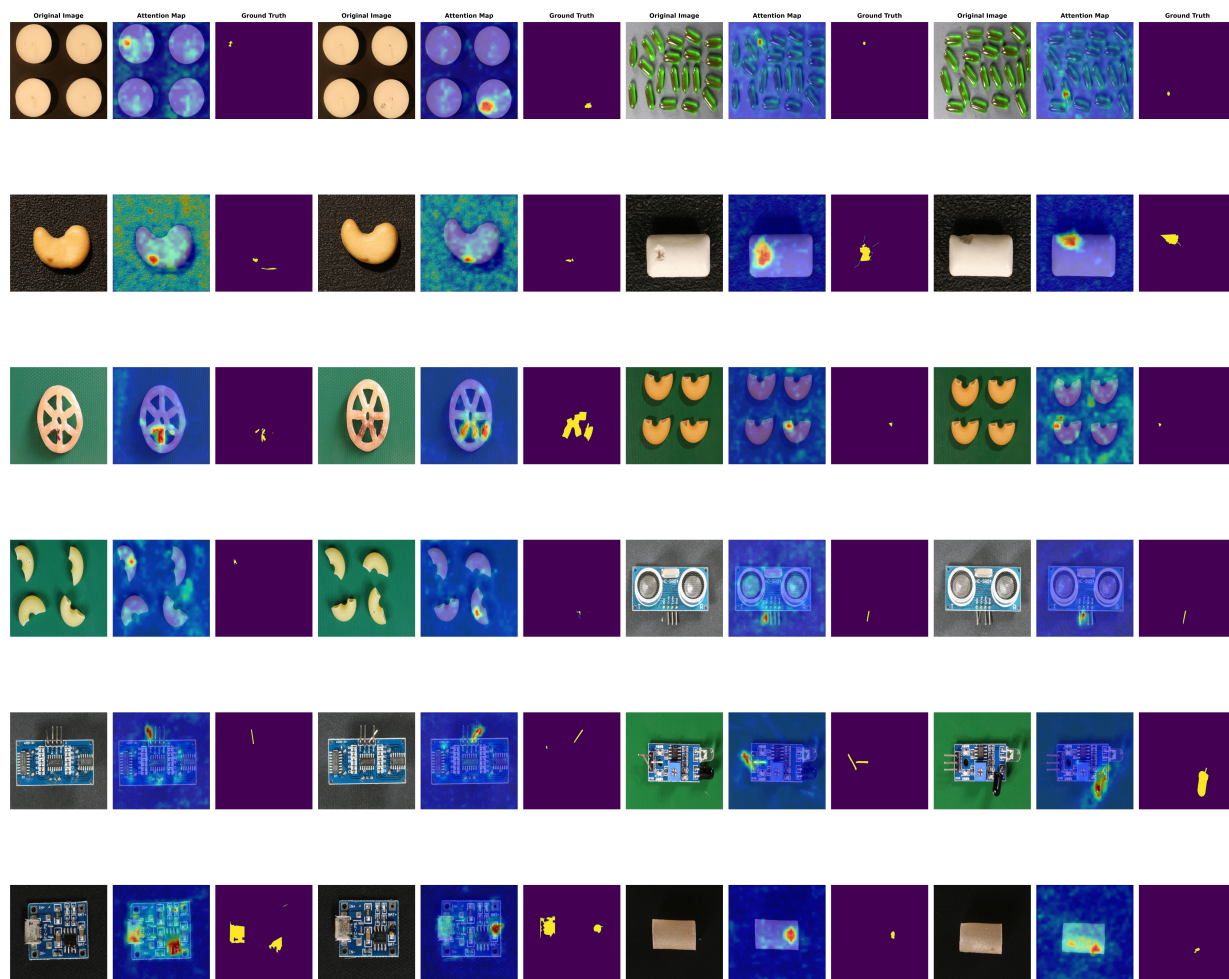


Figure 8. Qualitative results of our method on ViSA (Zou et al., 2022).

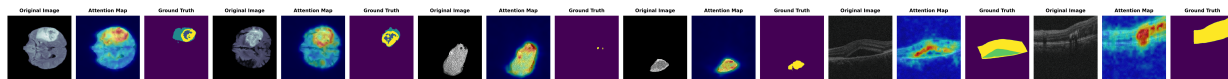


Figure 9. Qualitative results of our method on Universal Medical (He et al., 2024b).

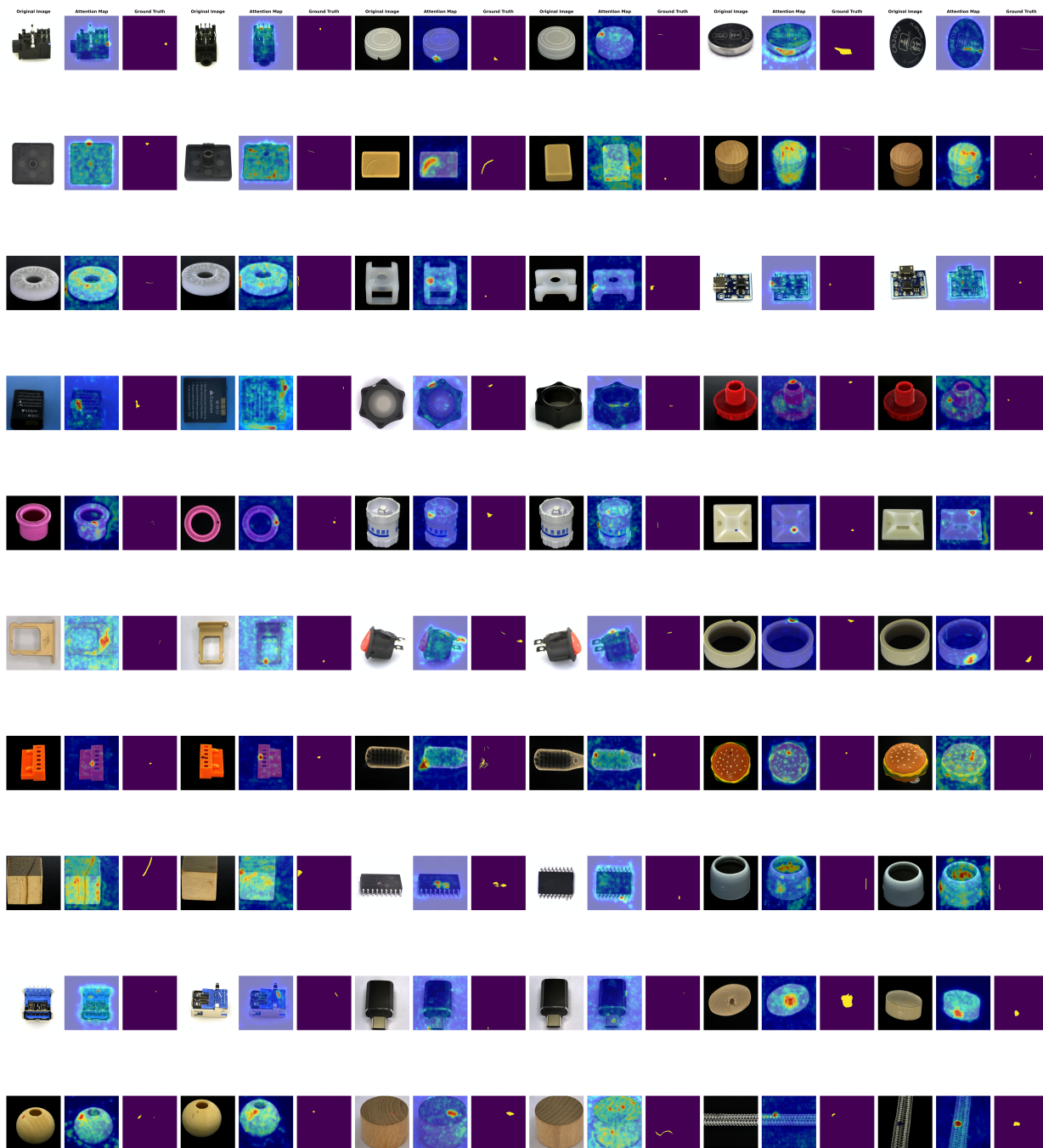


Figure 10. Qualitative results of our method on Real-IAD (Wang et al., 2024).